CrossMark

CAMBRIDGE
UNIVERSITY PRESS

Research Paper

Gaia EDR3 parallaxes of type I X-ray bursters and their implications on the models of type I X-ray bursts: A generic approach to the Gaia parallax zero point and its uncertainty

Hao Ding[1,2,*] , Adam T. Deller[1,2] and James C. A. Miller-Jones[3]

[1]Centre for Astrophysics and Supercomputing, Swinburne University of Technology, VIC 3122, Australia, [2]ARC Centre of Excellence for Gravitational Wave Discovery (OzGrav) and [3]International Centre for Radio Astronomy Research—Curtin University, WA 6845, Australia

Abstract

Light curves of photospheric radius expansion (PRE) bursts, a subset of type I X-ray bursts, have been used as standard candles to estimate the 'nominal PRE distances' for 63% of PRE bursters (bursters), assuming PRE burst emission is spherically symmetric. Model-independent geometric parallaxes of bursters provide a valuable chance to test models of PRE bursts (PRE models) and can be provided in some cases by Gaia astrometry of the donor stars in bursters. We searched for counterparts to 115 known bursters in the Gaia Early Data Release 3 and confirmed 4 bursters with Gaia counterparts that have detected ($>3\,\sigma$, prior to zero-point correction) parallaxes. We describe a generic approach to the Gaia parallax zero point as well as its uncertainty using an ensemble of Gaia quasars individually determined for each target. Assuming the spherically symmetric PRE model is correct, we refined the resultant nominal PRE distances of three bursters (i.e. Cen X − 4, Cyg X − 2, and 4U 0919 − 54) and put constraints on their compositions of the nuclear fuel powering the bursts. Finally, we describe a method for testing the correctness of the spherically symmetric PRE model using parallax measurements and provide preliminary results.

1. Introduction

A type I X-ray burst is rapid nuclear burning on the surface of a neutron star (NS) (e.g. Lewin van Paradijs, & Taam, 1993). Type I X-ray bursts happen when the accumulated 'nuclear fuel' accreted from the donor star onto the surface of the NS is sufficiently hot. In some cases, the radiation pressure becomes large enough to overcome the gravity of the NS, causing the photosphere to expand. This is followed by fallback of the photosphere after extending to its outermost point. This process of expansion and contraction of the photosphere is well characterised by double-peaked soft X-ray light curves. These particular type I X-ray bursts are called photospheric radius expansion (PRE) bursts.

According to Galloway et al. (2020), there are hitherto 115 recognised PRE bursters (see https://burst.sci.monash.edu/sources), which are all low mass X-ray binaries (LMXBs). PRE bursts can serve as standard candles (Basinska et al. 1984) based on the assumption that the luminosity of PRE bursts stays at the Eddington limit throughout the photospheric expansion and contraction. We refer to the distances estimated in this way as PRE distances. Using the standard assumption of spherically symmetric PRE burst emission, Galloway et al. (2020) constrained PRE distances for 73 PRE bursters (23 of which only have upper limits of PRE distances, see Table 8 of Galloway et al. 2020) based

on the theoretical Eddington luminosity calculated by Lewin et al. (1993). Hereafter, we refer to this spherically symmetric model as the simplistic PRE model, and the simplistic-PRE-model-based PRE distances as nominal PRE distances. Besides PRE models, a Bayesian framework has been recently developed to infer parameters, including the distance and the composition of nuclear fuel on the NS surface, for the type I X-ray burster SAX J1808.4-3658 (Goodwin et al. 2019), by matching the burst observables (such as burst flux and recurrence time) of non-PRE type I X-ray bursts with the prediction from a burst ignition model (Cumming & Bildsten 2000).

At least 43% of PRE bursters registered nominal PRE distances as their best constrained distances. The great usefulness of the simplistic PRE model calls for careful examination of its validity. There are several uncertainties in the simplistic PRE model. Firstly, according to Lewin et al. (1993), the Eddington luminosity measured by an observer at infinity

$$L_{\text{Edd},\infty} \propto \frac{M_{\text{NS}}}{1 + z(R_P)} \frac{1}{1 + X}, \tag{1}$$

depends on the NS mass M_{NS} and the gravitational redshift $z(R_P) = (1 - 2G_N M_{\text{NS}}/c^2 R_P)^{-1/2} - 1$ (where G_N and c stand for Newton's gravitational constant and speed of light in vacuum, respectively) at the photosphere radius R_P. To a greater degree, $L_{\text{Edd},\infty}$ hinges on the hydrogen mass fraction X of the nuclear fuel on the NS surface at the time of the PRE burst: hydrogen-free nuclear fuel corresponds to a $L_{\text{Edd},\infty}$ 1.7 times higher than nuclear fuel of cosmic abundances (Lewin et al., 1993). Secondly, the method assumes spherically symmetric emission. On the one

hand, PRE bursts per se are not necessarily spherically symmetric given that the NS in an LMXB is spinning and accretes via an accretion disk. On the other hand, even if PRE bursts are initially isotropic (assuming the nuclear fuel has spread evenly on the NS surface), propagation effects (such as the reflection from the surrounding accretion disk) would still potentially lead to anisotropy of PRE burst emission. Thirdly, for each PRE burster, the peak fluxes of its recognised PRE bursts vary, typically by 13% (Galloway et al. 2008).

Provided the uncertainties of the simplistic PRE model as well as the resultant nominal PRE distances, independent distance measurements for PRE bursters hold the key to testing the simplistic PRE model. By 2003, 12 PRE bursters in 12 globular clusters (GCs) had distances determined from RR Lyrae stars residing in the GCs; incorporating the distances with respective peak bolometric fluxes derived from X-ray observations of PRE bursts, Kuulkers et al. (2003) measured 12 observed Eddington luminosities, 9 of which are consistent with the theoretical value by Lewin et al., (1993). The independent check by Kuulkers et al. (2003) largely confirms the validity of the simplistic PRE model. The confirmation, however, is not conclusive due to the modest number of PRE bursters residing in GCs. Besides, this GC-only sample of PRE bursters might lead to some systematic offsets of the measured Eddington luminosities, as a result of potential systematic offsets of distances determined with RR Lyrae stars or X-ray flux decay that becomes more prominent in the dense regions of GCs.

Alternatively, geometric parallaxes of PRE bursters provided by the Gaia mission (Gaia Collaboration et al. 2016) can also be used to test the simplistic PRE model. This effort normally requires determination of Gaia parallax zero point π_0 for each PRE burster, as π_0 is found to be offset from 0 (Lindegren et al. 2018; 2021b). Recently, Arnason et al. (2021) (A21) has identified Gaia Data Release 2 (DR2) counterparts for 10 PRE bursters with Gaia parallaxes. After applying the Gaia DR2 global π_0 (Lindegren et al. 2018), A21 converted these parallaxes into distances, incorporating the prior information described in Bailer-Jones et al. (2018). A21 noted that the inferred distances of the 10 PRE bursters are systematically smaller than the nominal PRE distances estimated before 2008 (this discrepancy is relieved with the latest nominal PRE distances by Galloway et al. 2020, see the discussion in Section 4.2.1). However, due to the predominance of low-significance parallax constraints, this discrepancy is strongly dependent on the underlying Galactic distribution of PRE bursters (as is shown in Figure 3 of A21), which is far from well constrained. Moreover, adopting the Gaia DR2 global π_0, instead of one individually estimated for each source, would introduce an extra systematic error.

This work furthers the effort of A21 to test the simplistic PRE model with Gaia parallaxes of PRE bursters, making use of the latest Gaia Early Data Release 3 (EDR3, Brown et al. 2020). Unlike A21, this work only focuses on the PRE bursters with relatively significant Gaia parallaxes; we apply a locally determined π_0 for each PRE burster and probe the simplistic PRE model as well as the composition of nuclear fuel.

In addition to the above-mentioned motivation, Gaia astrometry of PRE bursters (hereafter simplified as bursters, when unambiguous) can provide more than geometric parallaxes (and hence distances). A Gaia counterpart of a burster also brings a reference position precise to sub-mas level, and possibly a detected proper motion as well. The latter can be combined with the parallax-based or model-dependent distance estimates to yield the burster's transverse space velocity (the transverse velocity with respect to its Galactic neighbourhood). The space velocity distribution of PRE bursters (or LMXBs) is important for testing binary evolution theories (see Tauris et al. 2017 as an analogy). Both reference position and proper motion can be used to confirm or rule out candidate counterparts at other wavelengths, especially when the immediate neighbourhood of a burster is crowded on a ~1" scale.

In this paper, all uncertainties are quoted at the $1\,\sigma$ confidence level unless otherwise stated; all sky positions are J2000 positions. As we mainly deal with Gaia photometric passbands (Jordi et al., 2010) in this work, a conventional optical passband is referred to in the form of Y*, while its magnitude is denoted by Y^*; by contrast, a Gaia passband is referred to in the form of Y band, and its magnitude is denoted by m_Y.

2. Gaia counterparts of PRE bursters with detected parallaxes

To be able to effectively refine nominal PRE distances, constrain the composition of nuclear fuel on the NS surface, and test the simplistic PRE model, we only search for Gaia counterparts with detected parallaxes π_1 ($> 3\,\sigma$, a criterion we apply throughout this paper). This cutoff leads to a smaller sample of PRE bursters compared to A21, which included many marginal parallax detections. Our search is based on the positions of 115 PRE bursters compiled in Table 1 of Galloway et al. (2020). For each PRE burster, we found its closest Gaia EDR3 source within 10."0 using TOPCAT[a]. From the resultant 110 candidates, we shortlisted 16 Gaia counterpart candidates with detected π_1. Among the 16 Gaia counterpart candidates, the Gaia counterparts for Cyg X − 2, Cen X − 4, and 4U 0919 − 54 have been recognised by VizieR (Ochsenbein, Bauer, & Marcout, 2000) in an automatic manner, simply based on the ≈1 mas angular distance (at the reference epoch year 2015.5 disregarding proper motion) that is comparable to the Gaia positional uncertainties (see Table 1); the Gaia counterpart for XB 2129+47 has been identified by A21.

To identify Gaia counterparts of PRE bursters from the remaining 12 candidates, we adopted a more complicated cross-match criterion, which requires the identification of an optical counterpart (either confirmed or potential) for the PRE burster. For an optical source $\mathcal{S}$ that is a confirmed or potential counterpart, we consider it associated with the Gaia source $\mathcal{G}$ if all the following conditions are met:

(i) $\mathcal{S}$ is sufficiently bright ($3 \leq G^* \leq 21^{\text{b}}$) for Gaia detection; the conventional apparent magnitude measured closest to G* band is looked at if G^* is not available (as compiled in Table 1);

(ii) $\mathcal{G}$ falls into the 1-$\sigma_{\mathcal{S}}$-radius circle around $\mathcal{S}$ (where the position of a confirmed radio or infrared counterpart of $\mathcal{S}$ would be adopted if it is more precise than the optical position);

(iii) $\mathcal{G}$ is the only Gaia source within the 5-$\sigma_{\mathcal{S}}$-radius circle around $\mathcal{S}$.

Here, to account for the effect of proper motion (and the smaller contribution of parallax), the position of the candidate has been extrapolated to the epoch at which the position of $\mathcal{S}$ was measured, with the astrometric parameters of $\mathcal{G}$ using the 'predictor

Table 1. Gaia EDR3 counterparts with detected parallaxes π_1 for 4 PRE bursters and NP Ser

Source name	$m^{*\ a_1}$ (mag)	$\sigma_{\mathcal{S}}^{a_2}$ (")	Gaia EDR3 counterpart	$m_{\rm B}^{a_3}$ (mag)	$\Delta_{\mathcal{S}-\mathcal{G}}^{a_4}$ (")	$R_1^{a_5}$ (")	Associated by?
NP Ser	$V^* = 17.42^{e_1}$	0.5^{e_2}	4146621775597340544	17.72	0.3	12	This work
Cyg X $-$ 2	–	–	1952859683185470208	–	–	–	VizieR[i]
Cen X $-$ 4	–	–	6205715168442046592	–	–	–	VizieR[i]
4U 0919 $-$ 54	–	–	5310395631798303104	–	–	–	VizieR[i]
XB 2129+47	–	–	1978241050130301312	–	–	–	A21[k]

[a1] Apparent magnitude at a conventional passband;
[a2] positional uncertainty (adding in quadrature uncertainties in both directions) of the source (see Section 2);
[a3] apparent magnitude at the Gaia B band (Jordi et al. 2010), which covers the conventional G*, V*, B* bands and part of the R* band;
[a4] angular separation between the source and its Gaia counterpart, where $\alpha_{\mathcal{G}}$ and $\delta_{\mathcal{G}}$ were extrapolated to the respective epoch of $\alpha_{\mathcal{S}}$ (and $\delta_{\mathcal{S}}$) using the astrometric parameters in Table 2 (see Section 2 for more explanation);
[a5] maximum search radius that contains only one Gaia source.
[e1] Deutsch et al. (1996);
[e2] Deutsch et al. (1999), where $\alpha_{\mathcal{S}} = 18^{\rm h}16^{\rm m}01\!\!\overset{\rm s}{.}380$, $\delta_{\mathcal{S}} = -14°02'\,11''34$ out of R-band CCD observation, with uncertainty radius of $0''5$ at 90 confidence, measured at MJD 50674.
[i] Ochsenbein et al. (2000);
[k] Arnason et al. (2021).

Table 2. Five astrometric parameters from Gaia EDR3 counterparts at year 2016.0 prior to calibration of Gaia parallaxes

Source name	$\alpha_{\mathcal{G}} \pm \sigma_\alpha$ (σ_α in mas)	$\delta_{\mathcal{G}}$	π_1 (mas)	$\mu_\alpha \equiv \dot{\alpha}\cos\delta$ (mas yr^{-1})	μ_δ (mas yr^{-1})
NP Ser	$18^{\rm h}16^{\rm m}01\!\!\overset{\rm s}{.}392863 \pm 0.07$	$-14°02'11\!\!\overset{''}{.}75580(6)$	0.69(8)	3.35(8)	$-6.97(6)$
Cyg X $-$ 2	$21^{\rm h}44^{\rm m}41\!\!\overset{\rm s}{.}152001 \pm 0.01$	$38°19'17\!\!\overset{''}{.}06138(1)$	0.068(19)	$-1.79(2)$	$-0.32(2)$
Cen X $-$ 4	$14^{\rm h}58^{\rm m}21\!\!\overset{\rm s}{.}93584 \pm 0.1$	$-31°40'08\!\!\overset{''}{.}40635(9)$	0.53(13)	0.84(15)	$-55.68(13)$
4U 0919 $-$ 54	$09^{\rm h}20^{\rm m}26\!\!\overset{\rm s}{.}471033 \pm 0.05$	$-55°12'24\!\!\overset{''}{.}47694(6)$	0.24(6)	$-5.77(7)$	2.24(8)
XB 2129+47	$21^{\rm h}31^{\rm m}26\!\!\overset{\rm s}{.}209631 \pm 0.06$	$47°17'24\!\!\overset{''}{.}44432(7)$	0.50(8)	$-2.34(8)$	$-4.23(8)$

mode' of pmpar (available at https://github.com/walterfb/pmpar). This extrapolation allows the evaluation of the same-epoch $\Delta_{\mathcal{S}-\mathcal{G}}$, the separation between $\mathcal{S}$ and $\mathcal{G}$, which is free from proper motion and parallax effects.

In principle, the apparent magnitude of $\mathcal{G}$ should match that of the optical counterpart of $\mathcal{S}$. However, making such a comparison is complicated by **(1)** the wide photometric passbands designed for the in-flight Gaia (Jordi et al. 2010) and **(2)** magnitude variability of stars.

On top of the 4 Gaia counterparts of PRE bursters (Cen X $-$ 4, Cyg X $-$ 2, 4U 0919 $-$ 54, and XB 2129+47) already recognised by VizieR and A21, we identified one Gaia counterpart with detected π_1 (from the remaining 12 objects), which was NP Ser (see Table 1). However, as we will discuss in Section 4.1, NP Ser is not the optical counterpart of GX 17 + 2, meaning that our final sample consists of 5 Gaia sources with detected π_1, of which 4 are PRE bursters.

Hereafter, the 5 Gaia sources are sometimes referred to as 'targets'. The (Gaia) B band covers the conventional G*, V*, B* bands and part of the R* band. According to Table 1, the magnitude V^* of NP Ser measured at conventional V* band generally agrees with $m_{\rm B}$ of its Gaia counterpart. The 5 astrometric parameters of the Gaia counterparts for the 4 PRE bursters and NP Ser are summarised in Table 2.

3. Calibration of Gaia parallaxes

Before being applied for scientific purposes, each of the Gaia parallaxes π_1 needs to be calibrated by determining its (Gaia) parallax zero point π_0, as π_0 has been shown to be systematically offset from zero (with an all-sky median of -0.02 mas for EDR3; Lindegren et al. 2021b). Previous studies have revealed the dependence of π_0 on sky position, apparent magnitude, and colour (Lindegren et al. 2018; Chen et al. 2018; Huang et al. 2021). Furthermore, Lindegren et al. (2021b) proposed that the position dependence of π_0 can be mostly attributed to the evolution of π_0 with respect to ecliptic latitude β and derived an empirical global solution for five-parameter (see Lindegren et al. 2021a for explanation) Gaia EDR3 sources and another such solution for six-parameter sources. While this approach is convenient to use, the empirical solutions do not provide an estimate of the uncertainty of π_0 and are only considered indicative (Lindegren et al. 2021b).

In this work, we attempted a new pathway of generic π_0 determination. Unlike the global empirical solutions, the new π_0 determination technique offers locally acquired π_0 and provides the uncertainty of the determined π_0. We estimated π_0 for the 5 targets using a subset of the agn_cross_id table publicised along with EDR3 (Klioner et al. in preparation). We selected 1 592 629 quasar-like sources (out of the 1 614 173 sources in the agn_cross_id table), which **(a)** have $m_{\rm B-R}$ (denoted as 'bp_rp' in EDR3) values and **(b)** show no detected ($>3\sigma$ level) proper motion in either direction. Hereafter, we refer to this subset of 1 592 629 sources as the quasar catalog, and its sources as background quasars or quasars (when unambiguous).

On the sky, spatial patterns of π_0 on angular scales of up to $\sim 10°$ are seen in Figure 2 of Lindegren et al. (2021b). We attempted different radius cuts (around each of the 5 targets) of

up to 40°, but found no clear evidence showing quasar parallaxes representative of the target π_0 beyond a 10° radius cut. In most cases, a 10° radius cut provides a sufficiently large sample of quasars for π_0 estimation. Hence, we only present analysis of quasars within 10° around each target.

3.1. A new pathway to parallax zero points

Our π_0 determination is solely based on the quasar catalog (of 1 592 629 sources). The vital step of (Gaia) parallax calibration (or π_0 determination) is to select appropriate quasars in the same sky region with similar G-band apparent magnitudes m_G and colours m_{B-R}. We implemented this selection for each of the 5 targets by applying 4 filters to the quasar catalog: the angular-distance filter, the β filter, the m_G filter, and the m_{B-R} filter. Once appropriate background quasars are chosen for each target, one can calculate π_0 as the weighted mean parallax of this 'sub-sample', and the formal uncertainty of π_0.

$$\tilde{\sigma}_{\pi_0} = \left(\sum_i \frac{1}{\sigma_i^2} \right)^{-\frac{1}{2}}. \tag{2}$$

(Equation (4.19) in Bevington & Robinson 2003), where σ_i is the (Gaia) parallax error of each background quasar in the sub-sample.

We parameterised **(1)** the angular-distance filter using the search radius r around the target, **(2)** the β filter using $\Delta \sin \beta$, the half width of the $\sin \beta$ filter centred about $\sin \beta^{\text{target}}$, **(3)** the m_G filter using $\underline{\Delta} m_G$, which stands for the relative half width (or $\Delta m_G / m_G^{\text{target}}$) of the m_G filter around m_G^{target}, and **(4)** the m_{B-R} filter using Δm_{B-R}, the half width of the m_{B-R} filter centred about m_{B-R}^{target}.

Hence, the problem of π_0 determination using background quasars can be reduced to searching for optimal filter parameters (for each target), i.e. r, $\Delta \sin \beta$, $\underline{\Delta} m_G$ and Δm_{B-R}. For this search, we investigated the marginalised relation between $s^*_{\pi_0}$ and each of the 4 parameters (see the top 4-panel block of Figure 1), where $s^*_{\pi_0} = s_{\pi_0}/s^{\text{glb}}_{\pi_0}$ stands for the weighted standard deviation of quasar parallaxes divided by its global value of 0.32 mas. To avoid small-sample fluctuations, Figure 1 starts at $N_{\text{quasar}} = 50$, or $N^{\text{start}}_{\text{quasar}} = 50$, which can also prevent overly small-sized sub-samples. To start with, we first introduce the $s^*_{\pi_0}$-to-$\underline{\Delta} m_G$ relation and explain its implications. Relations between $s^*_{\pi_0}$ and other 3 parameters can be interpreted in the same way.

Unlike $\tilde{\sigma}_{\pi_0}$, if a sufficiently large ($\gtrsim$50) background-quasar sample had no m_G dependence (as opposed to Lindegren et al. 2018; Lindegren et al. 2021b), $\log_{10} s^*_{\pi_0}$ would be expected to be largely independent to $\underline{\Delta} m_G$, and to fluctuate around the global value 0. This is clearly not the case for all of the 5 targets. From Figure 1, we found an obvious upward trend of $s^*_{\pi_0}$ with growing $\underline{\Delta} m_G$. This upward trend shows that background quasars with similar m_G around m_G^{target} tend to have similar parallaxes, which supports the m_G-dependence of π_0 stated in Lindegren et al. (2018); Lindegren et al. (2021b).

Using the same interpretation, we also investigated marginalised relations of $s^*_{\pi_0}$ with respect to each of the other 3 filter parameters. As can be seen in Figure 1, most fields show a (weak) colour dependence of π_0. For the two sky-position-related filter parameters, β dependence of π_0 is clearly found in the target fields of Cyg X − 2 and NP Ser, whereas the r dependence of π_0 is hardly noticeable in any of the 5 target fields. This contrast

reinforces the belief that the β dependence of π_0 contributes considerably to the position dependence of π_0 (Lindegren et al. 2021b). Additionally, $\log_{10} s^*_{\pi_0}$ converges to 0.0 ± 0.1 at $r = 10°$ in all target fields, which roughly agrees with our assumption that the r-dependence of π_0 becomes negligible beyond 10° search radius; in other words, quasar parallaxes at $r > 10°$ are almost not representative of the target π_0.

Knowing the way to interpret the relation between $s^*_{\pi_0}$ and each of the filter parameters, we can proceed to choose the optimal filter parameters. In choosing filter parameters, one wants the filtered sub-sample to have a consistently low level of $s^*_{\pi_0}$; meanwhile, one prefers a filtered sub-sample as large as possible to achieve reliable and precise π_0. To meet both demands is difficult when $s^*_{\pi_0}$ rises with a larger filter (as is the case for the m_G filter). In this regard, we created an index $w = A \log_{10} N_{\text{quasar}} - \log_{10} s^*_{\pi_0}$, where $A = (\log_{10} s^{*,\text{max}}_{\pi_0} - \log_{10} s^{*,\text{min}}_{\pi_0})/(\log_{10} N^{\text{max}}_{\text{quasar}} - \log_{10} N^{\text{start}}_{\text{quasar}})$ is a scaling factor. Instead of the minimum of $s^*_{\pi_0}$ or the maximum of N_{quasar}, we adopted the filter parameter at the peak of the index w (see the bottom 4-panel block of Figure 1), so that an optimised trade-off between $s^*_{\pi_0}$ and N_{quasar} can be reached. Using this consistent standard, we reached the parameter of each filter for each target (see Table 3).

After applying the 4 filters, we acquired a quasar sub-sample of N_{quasar} and $s^*_{\pi_0}$ for each target and obtained π_0 of the target from this sub-sample (see Table 3). Due to the relative paucity of quasars identified at low Galactic latitudes b (for the reasons discussed in Lindegren et al. 2021b), NP Ser, 4U 0919 − 54, and XB 2129+47 (all of which have $|b| < 4°$) receive relatively low values for N_{quasar} compared to Cen X − 4 ($b = 24°$), which partly lead to the relatively large $\tilde{\sigma}_{\pi_0}$. Nonetheless, we have shown that π_0 for targets at $|b| < 6°$ can be determined with nearby (on the sky) quasars. On the other hand, Cyg X − 2, despite being located at $b = -11°$, has the smallest N_{quasar} and the largest $\tilde{\sigma}_{\pi_0}$ among the 5 targets. This is mainly due to the relative rarity of bright quasars (Cyg X − 2 has $m_G = 14.7$ mag).

The negative $\log_{10} s^*_{\pi_0}$ of the quasar sub-sample for each target indicates that the sub-sample of (closely located, like-β, like-m_G, and like-m_{B-R}) quasars is representative of the target source. Despite this good representativeness, the $\tilde{\sigma}_{\pi_0}$ estimated with Equation (2) is still an under-estimate for the uncertainty of π_0, as the sub-sample has a spread in each parameter and does not represent the target perfectly. We estimated the weighted average m_G, m_{B-R}, and $\sin \beta$ of the quasar sub-sample (where the weighting is $1/\sigma_i^2$, see Equation (2) for the definition of σ_i), which are presented in Table 3 as $\overline{m_G}$, $\overline{m_{B-R}}$, and $\overline{\sin \beta}$, respectively. According to Table 3, there are residual offsets of $\sin \beta$, m_G, and m_{B-R} between the target and the average level of the sub-sample, which would result in extra systematic error for the π_0 estimates. To estimate this systematic error of π_0, we calculated the empirical parallax zero points for the targets (see Table 3) using `zero_point.zpt` (https://gitlab.com/icc-ub/public/gaiadr3_zeropoint, Lindegren et al. 2021b), noted as π_0^{emp}. In the same way, we also estimated the empirical parallax zero points for each quasar of the sub-sample, then derived the weighted average empirical parallax zero point of the sub-sample, noted as $\overline{\pi_0^{\text{emp}}}$ (see Table 3). The difference between π_0^{emp} and $\overline{\pi_0^{\text{emp}}}$ is taken as an estimate for the systematic error of π_0, which is added in quadrature to the $\tilde{\sigma}_{\pi_0}$ calculated with Equation (2).

No uncertainties are yet available for π_0^{emp}. Regardless, all of our π_0 are consistent with the empirical counterparts at the 2σ
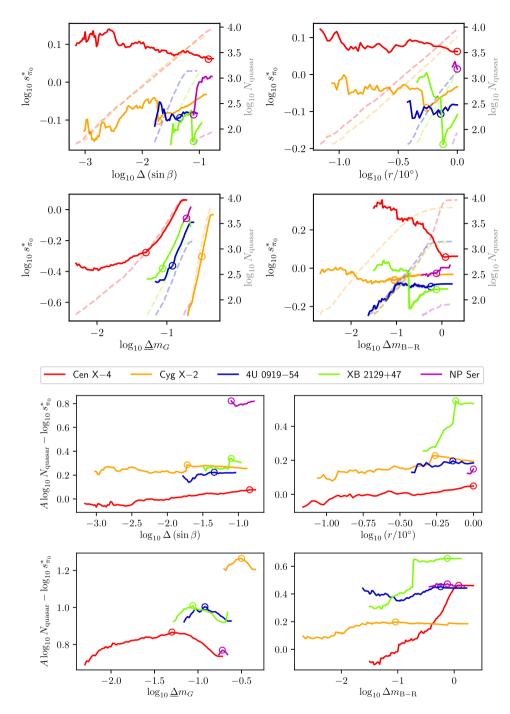
Figure 1. Top 4-panel block: The solid lines present the marginalised relations between $s^*_{\pi_0}$ of background quasars and 4 filter parameters: $\Delta \sin \beta$ (β denotes ecliptic latitude), search radius r around the target, $\underline{\Delta}m_G$ and $\Delta m_{B\text{-}R}$. Here, $s^*_{\pi_0} = s_{\pi_0}/s^{glb}_{\pi_0}$, where s_{π_0} and $s^{glb}_{\pi_0}$ represent the weighted standard deviation of quasar parallaxes and its global value (of the 1592629 quasars in the quasar catalog), respectively; $\Delta m_{B\text{-}R}|\Delta \sin \beta$ stands for the half width of the $m_{B\text{-}R}|\sin \beta$ filter centred around the $m^{target}_{B\text{-}R}|\sin \beta^{target}$ (used to pick like-$m_{B\text{-}R}$|like-β background quasars); $\underline{\Delta}m_G$ defines the half relative width of the m_G filter around m^{target}_G used to select like-m_G background quasars. The dashed curves lay out the marginalised relations between N_{quasar} and the 4 filter parameters, where N_{quasar} stands for number of remaining background quasars after being filtered. To avoid small-sample effect, the calculations start from $N_{quasar} = 50$, or $N^{start}_{quasar} = 50$. The dependence of π_0 on a variable (r, β, m_G, or $m_{B\text{-}R}$) is suggested if $s^*_{\pi_0}$ grows with a larger filter (such as the m_G dependence), and vice versa. **Bottom 4-panel block:** The marginalised relation between the index $w = A \log_{10} N_{quasar} - \log_{10} s^*_{\pi_0}$ and each filter parameter, where $A = (\log_{10} s^{*,max}_{\pi_0} - \log_{10} s^{*,min}_{\pi_0})/(\log_{10} N^{max}_{quasar} - \log_{10} N^{start}_{quasar})$ is a scaling factor. The maximum of w is chosen (circled out in both bottom and top blocks) as the 'optimal' filter parameter.

confidence level. We note that π^{emp}_0 is only used to estimate the systematic error of π_0 and is not adopted in the discussions that follow. The calibrated parallaxes $\pi_1 - \pi_0$ are summarised in Table 3.

Despite the overall consistency between π_0 and π^{emp}_0, it is noteworthy that all π_0 are larger than the π^{emp}_0 counterparts, which can be a coincidence of small-number statistics. Alternatively, knowing that most of the targets are situated at low b, it might indicate a systematic offset between quasar-sub-sample-based π_0 and π^{emp}_0 at low b. Interestingly, a recent parallax zero-point study based on $\sim$110 000 W Ursae Majoris variables showed that the W-Ursae-Majoris-variable-based π_0 are systematically larger than

Table 3. The information of the 4 filters (including search radius r, β filter, m_G filter, and $m_{B\text{-}R}$ filter, see Section 3.1 for explanation) and the parallax zero point π_0 calculated from the respective sub-sample of background quasars after applying the 4 filters. π_1 and $\pi_1 - \pi_0$ stand for uncalibrated parallaxes and calibrated parallaxes, respectively. $\overline{m_G}$, $\overline{m_{B\text{-}R}}$, and $\overline{\sin\beta}$ represent the respective weighted average value of the three filter parameters (see Section 3.1). N_{quasar} and $s^*_{\pi_0}$ (defined in Section 3.1) are reported for the filtered quasar sub-sample in each target field. The empirical parallax zero-point solutions for the targets calculated with `zero_point.zpt` (https://gitlab.com/icc-ub/public/gaiadr3_zeropoint) are provided as π_0^{emp}. The weighted average empirical parallax zero points of the sub-samples (see Section 3.1) are presented as $\overline{\pi_0^{\text{emp}}}$

Field	r	$\sin\beta^{\text{target}}$	$\Delta\sin\beta$	m_G^{target}	Δm_G	$m_{B\text{-}R}^{\text{target}}$	$\Delta m_{B\text{-}R}$	$\overline{m_G}$	$\overline{m_{B\text{-}R}}$	$\overline{\sin\beta}$
	(°)			(mag)		(mag)	(mag)			
Cen X − 4	10	−0.24	0.14	17.85	5.0%	1.59	1.20	18.00	0.74	−0.25
Cyg X − 2	5.5	0.74	0.02	14.70	31.6%	0.71	0.09	18.19	0.74	0.74
4U 0919 − 54	7.2	−0.90	0.05	17.15	12.0%	1.19	0.58	18.23	0.94	−0.93
XB 2129 + 47	7.6	0.84	0.08	17.58	8.7%	1.29	0.76	18.49	1.01	0.79
NP Ser	10	0.16	0.08	17.01	19.1%	1.51	0.76	17.61	1.57	0.16

Field	N_{quasar}	$\log_{10} s^*_{\pi_0}$	π_0^{emp}	$\overline{\pi_0^{\text{emp}}}$	π_0	π_1	$\pi_1 - \pi_0$
			(mas)	(mas)	(mas)	(mas)	
Cen X − 4	772	−0.27	−0.027	−0.026	−0.022 ± 0.006 ± 0.002	0.53 ± 0.13	0.55 ± 0.13
Cyg X − 2	32	−0.29	−0.030	−0.020	0.019 ± 0.024 ± 0.010	0.068 ± 0.019	0.050 ± 0.032
4U 0919 − 54	91	−0.33	−0.028	−0.027	−0.009 ± 0.013 ± 0.001	0.24 ± 0.06	0.25 ± 0.06
XB 2129 + 47	63	−0.37	−0.028	−0.019	0.004 ± 0.018 ± 0.009	0.50 ± 0.08	0.50 ± 0.08
NP Ser	40	−0.17	−0.032	−0.026	−0.008 ± 0.033 ± 0.006	0.69 ± 0.08	0.70 ± 0.09

the π_0^{emp} counterparts at low b (see Figure 3 of Ren et al. 2021). Hence, a future quasar-sub-sample-based study involving a large sample of targets (and other parallax zero-point studies by different approaches) will be essential for probing π_0^{emp} at low b. More specifically, if quasar-sub-sample-based π_0 at low b are confirmed to be systematically larger than the π_0^{emp} counterparts, then it is likely that π_0^{emp} is systematically under-estimated at low b.

4. Discussion

In this section, we discuss the implications of the 5 calibrated parallaxes $\pi_1 - \pi_0$ provided in Table 3.

4.1. NP Ser and GX 17 + 2 revisited

GX 17 + 2 is one of the brightest X-ray sources on the sky, from which 43 PRE bursts have been recorded (see Table 1 of Galloway et al. 2020 and references therein); its distance was estimated to be 7.3–12.6 kpc by treating its PRE bursts as standard candles (as explained in Section 1), where the distance uncertainty is dominated by the uncertain composition of the nuclear fuel (Galloway et al. 2020). The optical source NP Ser, $\approx 1.''0$ away from GX 17 + 2, was initially considered the optical counterpart of GX 17 + 2 (Tarenghi & Reina 1972), but the association has been ruled out, based on its sky-position offset from GX 17 + 2 (Deutsch et al. 1999) and its lack of optical variability (as expected for the optical counterpart of GX 17 + 2) (e.g. Davidsen et al. 1976; Margon 1978). Despite this, NP Ser was initially treated as a potential counterpart and the Gaia properties of NP Ser were analysed. Regardless of the non-association of NP Ser and GX 17 + 2, the complex sky region around GX 17 + 2 for optical/infrared observations (see Figure 2 of Deutsch et al. 1999 for example) merits

high-precision Gaia astrometry of NP Ser, which will facilitate future data analysis of optical/infrared observations of GX 17 + 2.

Using the astrometric parameters of NP Ser in Tables 2 and 3, we extrapolated the reference position of NP Ser (from the reference epoch 2016.0 yr, or MJD 57388) to MJD 47496, following the method described in Section 3.2 of Ding et al. (2020). The projected Gaia position of NP Ser is offset from the VLA position of GX 17 + 2 (see Table 2 of Deutsch et al. 1999) by $0.''95 \pm 0.''07$ at MJD 47496. Considering the distances to GX 17 + 2 and NP Ser, nuclear fuel with cosmic abundances (73% hydrogen) corresponds to the smallest PRE distance of 8.5 ± 1.2 kpc for GX 17 + 2 (Galloway et al. 2020); in comparison, the calibrated Gaia parallax of NP Ser is 0.70 ± 0.09 mas, corresponding to a distance of $1.44^{+0.21}_{-0.16}$ kpc, which establishes NP Ser as a foreground source of GX 17 + 2. The current sky-position offset between NP Ser and GX 17 + 2 depends on the proper motion of GX 17 + 2. Assuming GX 17 + 2 rotates around the Galactic centre in the Galactic disk with negligible peculiar velocity (with respect to the neighbourhood of GX 17 + 2), the apparent proper motion of GX 17 + 2 would be $\mu_\alpha = -3.5$ mas yr^{-1} and $\mu_\delta = -6.7$ mas yr^{-1} given a distance of 8.5 kpc (from the Earth). Based on this indicative proper motion of GX 17 + 2 and the Gaia ephemeris of NP Ser, NP Ser is currently (at MJD 59394) $1.''0$ away from GX 17 + 2 and continues to move away from GX 17 + 2 on the sky; accordingly, it would become easier with time to resolve GX 17 + 2 from the foreground NP Ser in optical/infrared observations.

4.2. Posterior distances and compositions of nuclear fuel for Cen X − 4, Cyg X − 2, and 4U 0919 − 54

Among the (calibrated) parallaxes $\pi_1 - \pi_0$ of the 4 PRE bursters (i.e. Cen X − 4, Cyg X − 2, 4U 0919 − 54, and XB 2129+47), $\pi_1 - \pi_0$ for Cen X − 4, 4U 0919 − 54 and XB 2129+47 are detected,

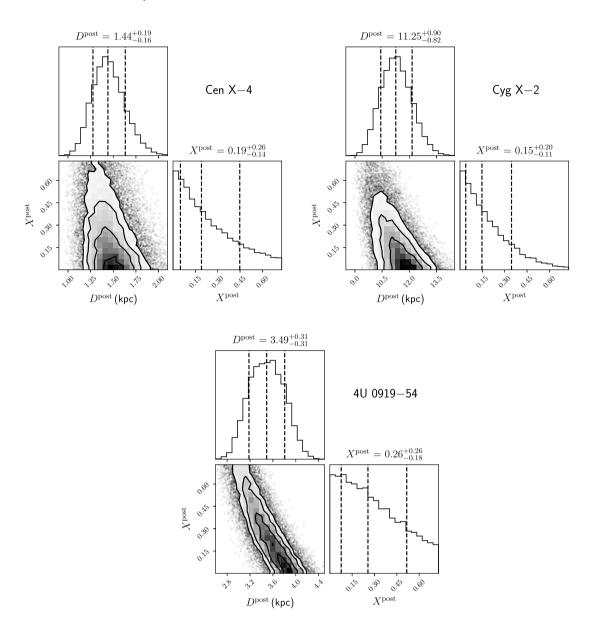**Figure 2.** 2-D histograms and marginalised 1-D histograms for posterior distance D^{post} and posterior mass fraction of hydrogen of nuclear fuel X^{post} simulated with `bilby` (Ashton et al. 2019) and plotted with `corner.py` (Foreman-Mackey 2016). The n-th contour in each 2-D histogram contains $1 - \exp\left(-n^2/2\right)$ of the simulated sample (Foreman-Mackey 2016). The vertical lines in the middle and two sides mark the median and central 68% of the sample, respectively.

whereas $\pi_1 - \pi_0$ of Cyg X$-$2 is weakly constrained. All PRE bursters except XB 2129+47 have nominal PRE distances published that are inferred from their respective PRE bursts (see Table 4 for PRE distances and their references). Using Bayesian inference, we can incorporate the parallax of a PRE burster with its nominal PRE distance to constrain the composition of nuclear fuel and refine the nominal PRE distance.

In Section 1, we have mentioned that the Eddington luminosity (measured by an observer at infinity) $L_{Edd,\infty}$ varies with NS mass M_{NS} and photosphere radius R_P (see Equation (1)). In practice, the bolometric flux at the 'touchdown' (when the photosphere drops back to the NS surface) of a PRE burst is compared to the theoretical $L_{Edd,\infty}$ at $R_P = R_{NS}$ (where R_{NS} stands for NS radius) to calculate the nominal PRE distance (Galloway et al. 2020). Therefore, the theoretical $L_{Edd,\infty}$ should change with M_{NS} and R_{NS}, which is, however, not taken into account in this work. We note

that, following Galloway et al. (2020), we assume $M_{NS} = 1.4\,M_\odot$ and $R_{NS} = 11.2$ km (Steiner et al. 2018) for all PRE bursters.

4.2.1. Bayes factor between two ends of the composition of nuclear fuel

As mentioned in Section 1, the Eddington luminosity of PRE bursts depends on the composition of nuclear fuel (accreted onto the NS surface from its companion) at the time of the outburst. This composition is normally parameterised by X, the mass fraction of hydrogen in nuclear fuel at the time of a PRE burst, which generally ranges from 0 to $\approx 73\%$, the cosmic mass fraction of hydrogen. As the result of the dynamic nucleosynthesis process during accretion, X varies from one PRE burst to another, but is always smaller than the hydrogen mass fraction of the donor star.

Table 4. Bayes factor $K = K_{X=0}^{X=0.7} = P(\pi_1 - \pi_0 | X = 0.7)/P(\pi_1 - \pi_0 | X = 0)$ (ratio of two conditional probabilities), where X refers to the mass fraction of hydrogen of the nuclear fuel

PRE burster	$D(X=0)$ (kpc)	$\log_{10} K$	D^{post} (kpc)	X^{post}
Cen X $-$ 4	$1.2(3)^a$	-0.83	$1.4(2)$	$0.2^{+0.3}_{-0.1}$
Cyg X $-$ 2	$11.6(9)^b$	-0.51	$11.3^{+0.9}_{-0.8}$	$0.2^{+0.2}_{-0.1}$
4U 0919 $-$ 54	$3.9(2)^b$	-0.39	$3.5(3)$	$0.3^{+0.3}_{-0.2}$

[a]Chevalier et al. (1989);
[b]Galloway et al. (2020).

X can be roughly predicted by the theoretical ignition models of X-ray bursts and mainly depends on the local accretion rate $\dot{m}$ (e.g. Fujimoto, Hanawa, & Miyaji, 1981).

Nominal PRE distances for $X = 0$, denoted as D_0, are summarised in Table 4 along with their references. At any given X, the nominal PRE distance $D_X = D_0/\sqrt{X+1}$ (Lewin et al. 1993). As the fractional uncertainty of a nominal PRE distance measurement is independent of X, $\sigma_X = \sigma_0/\sqrt{1+X}$, where σ_0 and σ_X represent the uncertainty of the nominal PRE distance at $X = 0$ and at a given X, respectively.

As our first attempt to constrain X, we used the calibrated Gaia parallax of each PRE burster to determine which value of X is more likely for the burster –0.73 or 0. We calculated the Bayes factor $K = K_{X=0}^{X=0.7}$ using

$$
K = \frac{\mathrm{P}(\pi_1 - \pi_0 | X = 0.7)}{\mathrm{P}(\pi_1 - \pi_0 | X = 0)}
$$
$$
= \frac{\int_0^\infty \frac{1}{\sigma_{0.7}} \exp\left[-\frac{1}{2}\left(\frac{1/D - \mu_\pi}{\sigma_\pi}\right)^2 - \frac{1}{2}\left(\frac{D - D_{0.7}}{\sigma_{0.7}}\right)^2\right] \mathrm{d}D}{\int_0^\infty \frac{1}{\sigma_0} \exp\left[-\frac{1}{2}\left(\frac{1/D - \mu_\pi}{\sigma_\pi}\right)^2 - \frac{1}{2}\left(\frac{D - D_0}{\sigma_0}\right)^2\right] \mathrm{d}D}, \quad (3)
$$

where $\pi_1 - \pi_0 = \mu_\pi \pm \sigma_\pi$, $D|_{X=0.7} = D_{0.7} \pm \sigma_{0.7}$ and $D|_{X=0} = D_0 \pm \sigma_0$. For the calculation of $K_{X=0}^{X=0.7}$, we did not use any Galactic prior (see Equation (4) for explanation), as the extra constraint given by a Galactic prior is negligible when X is fixed. The results of $K_{X=0}^{X=0.7}$ are presented in Table 4.

Among the three $\log_{10} K_{X=0}^{X=0.7}$ values, the one for Cen X $-$ 4 is the most offset from 0, which suggests the calibrated parallax of Cen X $-$ 4 substantially (when $0.5 < |\log_{10} K_{X=0}^{X=0.7}| < 1$, Kass & Raftery 1995) favours $X = 0$ over $X = 0.7$. Merely 2 PRE bursts have ever been observed from Cen X $-$ 4 in 1969 (Belian et al. 1972) and 1979 (Matsuoka et al. 1980). The long intervals between PRE bursts of Cen X $-$ 4 imply small accretion rates and low X at the time of PRE bursts, despite hydrogen signatures observed from its donor star (e.g. Shahbaz, Watson, & Dhillon, 2014). This expectation is confirmed by the $\log_{10} K_{X=0}^{X=0.7}$ of Cen X $-$ 4.

It is noteworthy that hydrogen-poor nuclear fuel at the time of PRE bursts is also favoured for Cyg X $-$ 2 and 4U 0919 $-$ 54. In fact, the previous independent test of the simplistic PRE model using GC PRE bursters also suggests hydrogen-poor nuclear fuel at the time of PRE bursts for the majority of the 12 GC PRE bursters (Kuulkers et al. 2003). The statistical inclination towards low X, if confirmed with a larger sample of PRE bursters, might be partly attributed to a selection effect explained as follows.

For each PRE burster, only the brightest PRE bursts are selected to calculate its nominal PRE distance (Galloway et al. 2008; 2020; Chevalier et al. 1989). This selection criterion results in a nominal PRE distance that tends to decrease with time as brighter bursts

are discovered. This tendency is clearly shown by the fact that almost all the nominal PRE distances registered in Table 9 of Galloway et al. (2008) are larger than their counterparts in Table 8 of Galloway et al. (2020). If we assume the variability of observed fluxes of PRE bursts is mainly caused by the fluctuation of X (at the time of different PRE bursts), the selection criterion of PRE bursters would lead to an increasingly biased PRE-burst sample that is more likely low-X. This selection effect would have a big impact on the X of the frequent PRE burster Cyg X $-$ 2 (see n_{burst} in Table 1 of Galloway et al. 2020), but less so for 4U 0919 $-$ 54 and Cen X $-$ 4. A low X of 4U 0919 $-$ 54 (if confirmed in the future) can be explained by the suggestion that the donor star of 4U 0919 $-$ 54 is likely a helium white dwarf (in't Zand et al. 2005). On the other hand, the revised nominal PRE distances of PRE bursters (Galloway et al. 2020) relieve the tension between the pre-2008 nominal PRE distances (see the references in Table 1 of A21) and the Gaia DR2 distances (A21), as mentioned in Section 1.

4.2.2. Refining nominal PRE distances and compositions of nuclear fuel

To better understand the statistical properties of X (and to refine the PRE distance), we subsequently constrained both X and the nominal PRE distance D of each PRE burster with its calibrated parallax in a Bayesian way. The 2-D joint probability distribution (JPD) we applied is

$$
\phi = \phi(D, X \mid \pi_1 - \pi_0, D_0)
$$
$$
\propto \phi(\pi_1 - \pi_0, D_0 \mid D, X)
$$
$$
\propto \rho(D) \exp\left[-\frac{1}{2}\left(\frac{\frac{1}{D} - \mu_\pi}{\sigma_\pi}\right)^2 - \frac{1}{2}\left(\frac{D - \frac{D_0}{\sqrt{X+1}}}{\frac{\sigma_0}{\sqrt{X+1}}}\right)^2\right],
$$
$$
(D > 0 \text{ and } X \in [0, 0.73]), \quad (4)
$$

where $\rho(D)$ represents the Galactic prior term, i.e., the prior probability of finding a PRE burster at a distance D along a given line of sight. We approached ρ by the Galactic mass distribution of LMXBs, which can be calculated with Equation (5) of Atri et al. (2019) using parameters provided by Grimm et al. (2002); Atri et al. (2019). Among the three components of the Galactic mass density (i.e. ρ_{bulge}, ρ_{disk}, and ρ_{sphere}, see Grimm et al. 2002 for explanations), the Galactic-disk component ρ_{disk} dominates the Galactic mass density budget for LMXBs at the light of sight to any of the three PRE bursters. Therefore, for this work alone, we adopted ρ_{disk} (see Equation (5) of Grimm et al. 2002) as the Galactic prior term ρ.

Following the JPD, we simulated posterior $\{D, X\}$ pairs (hereafter referred to as D^{post} and X^{post}), using bilby[c] (Ashton et al. 2019). For this simulation, we adopted a uniform distribution between 0 and 0.73 for X and a uniform distribution between 0 and 50 kpc for D (where using a larger upper limit of D does not change the result). Based on the marginalised probability density functions (PDFs) of the simulated $\{D^{\mathrm{post}}, X^{\mathrm{post}}\}$ chain, we estimated D^{post} and X^{post}, which are presented in Figure 2 and Table 4.

In general, the conversion of parallax to distance depends on the adopted Galactic prior (Bailer-Jones 2015). As an example, A21 found that the application of different Galactic priors (e.g. Bailer-Jones et al. 2021; Atri et al. 2019) results in inconsistent
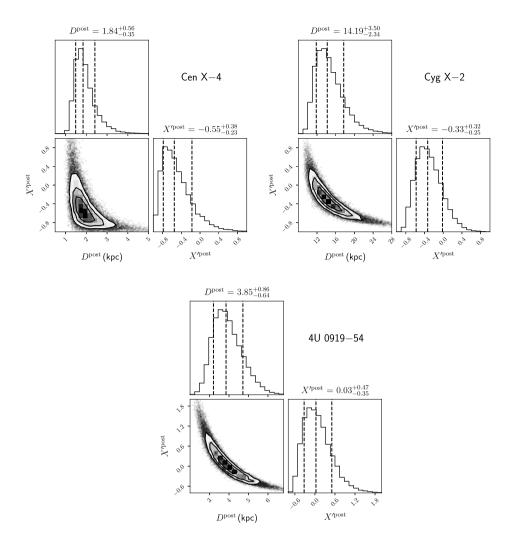
[c]https://lscsoft.docs.ligo.org/bilby/

Figure 3. 2-D histograms and marginalised 1-D histograms of posterior distance D^{post} and X'^{post} (defined in Section 4.3) simulated with `bilby` (Ashton et al. 2019) and plotted with `corner.py` (Foreman-Mackey 2016). The n-th contour in each 2-D histogram contains $1 - \exp\left(-n^2/2\right)$ of the simulated sample (Foreman-Mackey 2016). The vertical lines in the middle and two sides mark the median and central 68% of the sample, respectively.

distances (see Figure 3 of A21). Unlike A21, we applied an extra constraint on D provided by the PRE distance (see Equation (4)), which gives a handle on X and improves the constraint on D. With this extra constraint, the dependence on the Galactic prior becomes negligible for all of the three PRE bursters: their D^{post} and X^{post} stay almost the same without the $\rho(D)$ term.

The PDFs of X provide richer information on X than $K_{X=0}^{X=0.7}$. As expected from $K_{X=0}^{X=0.7}$, the PDF of X for Cen X$-$4 favours a hydrogen-poor nature of nuclear fuel. In addition to the new constraint we put on X, the nominal PRE distance of each PRE burster incorporating the parallax information is supposed to be more reliable (though not necessarily more precise). We note that the refined nominal PRE distances are still model dependent; their accuracies are subject to the validity of the simplistic PRE model.

4.3. A roadmap for testing the simplistic PRE model with parallax measurements

The discussion in Section 4.2 is based on the correctness of the simplistic PRE model. Now we discuss the potential feasibility of using parallaxes (of PRE bursters) to test the simplistic PRE model.

We first define the PRE distance correction factor η ($\eta > 0$) using the relation

$$D_X = \eta \, \frac{D_0}{\sqrt{X+1}}, \tag{5}$$

where D_0 stands for the nominal PRE distance at $X = 0$ (derived from the simplistic PRE model), and D_X refers to the 'true' distance. If the simplistic PRE model is correct, then $\eta = 1$. However, $\eta \neq 1$ is possible due to various causes including the stochasticity of PRE burst luminosity and anisotropy of PRE burst emission (e.g. Sztajno et al. 1987). The latter cause implies η to be geometry dependent (e.g. viewing-angle-related); if all PRE bursters have different geometry-dependent η, a search for a global deviation of η from unity with a sample of PRE bursters would be less practical. Nevertheless, it remains practical to constrain η on an individual basis. One way to make this constraint is using the generalised X, defined as

$$X' + 1 = \frac{X+1}{\eta^2}. \tag{6}$$

Table 5. D^{post} and X'^{post} (see Section 4.3) inferred from the Galactic prior $\rho(D)$ of Equation (4), in comparison to the counterparts (noted as $\tilde{D}^{\text{post}}$ and $\tilde{X}'^{\text{post}}$) given $\rho(D) = 1$

PRE burster	D^{post} (kpc)	$\tilde{D}^{\text{post}}$ (kpc)	X'^{post}	$\tilde{X}'^{\text{post}}$
Cen X $-$ 4	$1.8^{+0.6}_{-0.4}$	$1.8^{+0.6}_{-0.3}$	$-0.55^{+0.38}_{-0.23}$	$-0.54^{+0.38}_{-0.24}$
Cyg X $-$ 2	14^{+4}_{-2}	18^{+13}_{-6}	$-0.3(3)$	$-0.6^{+0.5}_{-0.3}$
4U 0919 $-$ 54	$3.9^{+0.9}_{-0.6}$	$4.1^{+1.2}_{-0.8}$	$0.0^{+0.5}_{-0.4}$	$-0.1^{+0.5}_{-0.4}$

Table 6. Predicted parallax (π_1) uncertainties $\hat{\sigma}_{\pi_1}$ for Cen X $-$ 4, Cyg X $-$ 2, and 4U 0919 $-$ 54 obtained with simulations (see Appendix A for details). For comparison, real values of $\sigma_{\pi_1}^{\text{DR2}}$ are provided as $\sigma_{\pi_1}^{\text{DR2}}$

PRE burster	$\hat{\sigma}_{\pi_1}^{\text{DR2}}$ (mas)	$\sigma_{\pi_1}^{\text{DR2}}$ (mas)	$\sigma_{\pi_1}^{\text{EDR3}}$ (mas)	$\hat{\sigma}_{\pi_1}^{\text{DR4}}$ (mas)	$\hat{\sigma}_{\pi_1}^{\text{ext *}}$ (mas)
Cen X $-$ 4	0.16	0.15	0.13	0.10	0.07
Cyg X $-$ 2	0.024	0.024	0.019	0.014	0.010
4U 0919 $-$ 54	0.08	0.07	0.06	0.05	0.03
XB 2129+47	0.10	0.09	0.08	0.06	0.04

* we adopt an indicative 5-yr extension on top of the Gaia 5-yr mission.

Accordingly, $D_X = D_0/\sqrt{X' + 1}$. Thanks to the same mathematical formalism, we can re-use Equation (4) as the JPD for statistical analysis, except that the domain of X' is widened to $X' > -1$.

The simulated $\{D^{\text{post}}, X'^{\text{post}}\}$ chain (posterior D and X') is depicted in Figure 3. If the simplistic PRE model is correct, then $\eta = 1$; as a result, X' is supposed to fall into the 'standard' domain of $[0, 0.73]$. None of the three PDFs of X' decisively rules out X' from this standard domain. However, we notice $X' < 0$ at 90% confidence for Cen X $-$ 4, which moderately disfavours the simplistic PRE model.

As the domain of X' is broadened from that of X, the fractional precision of D^{post} becomes predominantly reliant on that of the parallax. In this regime, D^{post} and X'^{post} become more dependent on the adopted Galactic prior. To understand the degree of this dependence, we re-estimated D^{post} and X'^{post} after resetting the Galactic prior to $\rho(D) = 1$, which are summarised in Table 5. For Cyg X $-$ 2 with insignificant $\pi_1 - \pi_0$, the dependence on the Galactic prior is evident, despite the consistency between the two sets of D^{post} and X'^{post}. For Cen X $-$ 4 and 4U 0919 $-$ 54 both having relatively significant $\pi_1 - \pi_0$, the degree of the dependence varies with the Galactic coordinates of the targets. In particular, we found the D^{post} and X'^{post} of Cen X $-$ 4 are robust against the selection of Galactic priors in Equation (4).

Using X' as a probe of the simplistic PRE model has the advantage of being independent of the PDF for X, which is usually not available. Future D_0 and $\pi_1 - \pi_0$ measurements with higher precision will sharpen the above test of the simplistic PRE model. Lower fractional uncertainty of $\pi_1 - \pi_0$ will not only reduce the strong correlation between D^{post} and X'^{post} for Cyg X $-$ 2 and 4U 0919 $-$ 54 (shown in Figure 3) but also lessen the dependence of inferred D^{post} and X'^{post} on the adopted Galactic prior. On the other hand, constraining X at PRE bursts independently (with, for example, ignition models of X-ray bursts) is the key to singling out η. Given that the simplistic PRE model is not significantly disfavoured by any of the 3 PRE bursters, the refined distances in Table 4 (based on the correctness of the simplistic PRE model) are still valid.

4.4. Future prospects

The potential of constraining X and testing the simplistic PRE model using Gaia parallaxes of PRE bursters hinges on the achievable parallax uncertainties. Future Gaia data releases include Gaia Data Release 4 (DR4) (for the 5-yr data collection) and the data release after extended observations of up to 5.4 yr (https://www.cosmos.esa.int/web/gaia/release). We predict the achievable parallax (π_1) and proper motion uncertainties of Cen X $-$ 4 for future Gaia data releases using the simulation method detailed in Appendix A. In the same way, we estimated the predicted π_1 uncertainty $\hat{\sigma}_{\pi_1}$ of Cyg X $-$ 2, 4U 0919 $-$ 54, and XB

2129+47 for future data releases and DR2, which are listed in Table 6. The predicted π_1 uncertainties for DR2, denoted as $\hat{\sigma}_{\pi_1}^{\text{DR2}}$, generally agree with the real values $\sigma_{\pi_1}^{\text{DR2}}$ (see Table 6). In general, our simulation shows Gaia parallax and proper motion precision improves with observation time t at roughly $t^{-1/2}$ and $t^{-3/2}$, respectively.

According to Table 3, the future parallax uncertainty of Cyg X $-$ 2 will be predominantly limited by the uncertainty of π_0, or σ_{π_0}. For this target, improvement in the estimation of the zero-point parallax correction and its uncertainty – which is challenging due to the relative brightness of the source – is essential. In comparison, the σ_{π_1} of Cen X $-$ 4, 4U 0919 $-$ 54, and XB 2129+47 dominates the respective error budget of the calibrated parallax $\pi_1 - \pi_0$. Therefore, one can expect $\pi_1 - \pi_0$ of Cen X $-$ 4, 4U 0919 $-$ 54, and XB 2129+47 to be potentially 1.9 times more precise (than EDR3) at the end of the extended Gaia mission (with 10-yr data), which would promise better constraints on X and X' for Cen X $-$ 4 and 4U 0919 $-$ 54. On the other hand, to constrain X and X' for XB 2129+47 with its already relatively precise Gaia parallax will require more PRE bursts to be detected from XB 2129+47. Apart from Gaia astrometry, radio observations of PRE bursters during their outbursts using very long baseline interferometry technique can also potentially measure geometric parallaxes of PRE bursters, hence serving the same scientific goals outlined in this paper.

This work only deals with the simplistic PRE model, the hitherto most impactful PRE model. As is mentioned in Section 1, PRE models are not the only pathway to the distances of type I X-ray bursters. Bayesian inference based on a burst ignition model (Cumming & Bildsten 2000) was recently realised to estimate parameters including X and D (Goodwin et al. 2019). We believe such inferences will be made for more type I X-ray bursters in the near future. In Bayesian analysis based on burst ignition models (e.g. Cumming & Bildsten 2000; Woosley et al. 2004), model-independent geometric parallaxes will serve as prior knowledge and help refine the inferred parameters including D and X; the parallaxes can also judge which burst ignition model is more likely correct with a Bayes factor analysis.

Finally, we reiterate that we have assumed $M_{\text{NS}} = 1.4\,M_\odot$ and $R_{\text{NS}} = 11.2$ km for all PRE bursters. Therefore, strictly speaking, η should also reflect the deviation of M_{NS} and R_{NS} from their respective assumed values. Though a large deviation of M_{NS} from $1.4\,M_\odot$ is rare, it is not impossible (Shao et al. 2020). In general, $L_{\text{Edd},\infty}$ would increase with larger M_{NS} and R_{NS} (see Equation (1)). For example, $L_{\text{Edd},\infty}(M_{\text{NS}} = 2, R_{\text{NS}} = 15)$ is 40% greater than $L_{\text{Edd},\infty}(M_{\text{NS}} = 1.4, R_{\text{NS}} = 11.2)$. Such a $L_{\text{Edd},\infty}$ would correspond to $X' = -0.29$ assuming $X = 0$ and the simplistic PRE model is correct. This value is consistent with $X' = -0.55^{+0.38}_{-0.23}$ for Cen X $-$ 4.

Given that the NS mass distribution is relatively well constrained compared to the NS radius distribution, it is possible to constrain the NS radius of a PRE burster in a Bayesian framework (slightly different from this work) provided prior knowledge of X, D, and M_{NS}, assuming the simplistic PRE model is correct.

5. Conclusion

This work joins the few previous efforts to determine the Gaia parallax zero-point π_0 for a single source using nearby (on the sky) background quasars. We provide a new template for π_0 determination (which also includes the π_0 uncertainty) approached by the weighted standard deviation of quasar parallaxes with respect to the filter parameters (see Section 3). This work focuses on the small sample of PRE bursters with detected Gaia parallaxes π_1. A future work will apply the new template to a larger sample of targets, which can enable a comprehensive comparison with zero-parallax points estimated in other ways.

We also introduce a Bayesian framework to test the simplistic PRE model with parallaxes of PRE bursters on an individual basis. Though no parallax of the PRE bursters decisively disfavours the simplistic PRE model, the model is disfavoured by the current Cen X − 4 parallax at 90% confidence. At the end of the extended Gaia mission with 10-yr data, we expect the parallax precision to improve by a factor of 1.9, which will sharpen the test of the simplistic PRE model. This test will also considerably benefit from an independent determination of X (hydrogen mass fraction of nuclear fuel), which we highly encourage.

References

Arnason, R., Papei, H., Barmby, P., Bahramian, A., & Gorski, M. 2021, MNRAS
Ashton, G., et al. 2019, ApJS, 241, 27
Atri, P., et al. 2019, MNRAS, 489, 3116
Bailer-Jones, C. A. 2015, PASP, 127, 994
Bailer-Jones, C., Rybizki, J., Fouesneau, M., Mantelet, G., & Andrae, R. 2018, AJ, 156, 58
Bailer-Jones, C., Rybizki, J., Fouesneau, M., Demleitner, M., & Andrae, R. 2021, AJ, 161, 147
Basinska, E. M., Lewin, W. H. G., Sztajno, M., Cominsky, L. R., & Marshall, F. J. 1984, ApJ, 281, 337
Belian, R., Conner, J., & Evans, W. 1972, ApJ, 171, L87
Bevington, P. R., & Robinson, D. K. 2003, Data Reduction and Error Analysis (McGraw-Hill Education)
Brown, A., Vallenari, A., Prusti, T., de Bruijne, J., Babusiaux, C., Biermann, M., Collaboration, G., et al. 2020, arXiv preprint arXiv:2012.01533
Chen, S., Richer, H., Caiazzo, I., & Heyl, J. 2018, ApJ, 867, 132
Chevalier, C., Ilovaisky, S., Van Paradijs, J., Pedersen, H., & Van der Klis, M. 1989, A&A, 210, 114

Cumming, A., & Bildsten, L. 2000, ApJ, 544, 453
Davidsen, A., Malina, R., & Bowyer, S. 1976, ApJ, 203, 448
Deutsch, E. W., Margon, B., Wachter, S., & Anderson, S. F. 1996, ApJ, 471, 979
Deutsch, E. W., Margon, B., Anderson, S. F., Wachter, S., & Goss, W. M. 1999, ApJ, 524, 406
Ding, H., Deller, A. T., Freire, P., Kaplan, D. L., Lazio, T. J. W., Shannon, R., & Stappers, B. 2020, ApJ, 896, 85
Foreman-Mackey, D. 2016, J. Open Sour. Softw., 1, 24
Fujimoto, M., Hanawa, T., & Miyaji, S. 1981, ApJ, 247, 267
Gaia Collaboration et al. 2016, A&A, 595, A1
Galloway, D. K., Muno, M. P., Hartman, J. M., Psaltis, D., & Chakrabarty, D. 2008, ApJS, 179, 360
Galloway, D. K., et al. 2020, ApJS, 249, 32
Goodwin, A., Galloway, D., Heger, A., Cumming, A., & Johnston, Z. 2019, MNRAS, 490, 2228
Grimm, H.-J., Gilfanov, M., & Sunyaev, R. 2002, A&A, 391, 923
Huang, Y., Yuan, H., Beers, T. C., & Zhang, H. 2021, ApJ, 910, L5
Jordi, C., et al. 2010, A&A, 523, A48
Kass, R. E., & Raftery, A. E. 1995, J. Amer. Stat. Assoc., 90, 773
Kuulkers E., den Hartog, P. R., in't Zand, J. J. M., Verbunt, F. W. M., Harris, W. E., & Cocchi, M. 2003, A&A, 399, 663
Lewin, W. H. G., van Paradijs, J., & Taam, R. E. 1993, Space Sci. Rev., 62, 223
Lindegren, L., et al. 2018, A&A, 616, A2
Lindegren, L., et al. 2021a, A&A, 649, A2
Lindegren, L., et al. 2021b, A&A, 649, A4
Margon, B. 1978, ApJ, 219, 613
Matsuoka, M., et al. 1980, ApJ, 240, L137
Ochsenbein, F., Bauer, P., & Marcout, J. 2000, A&AS, 143, 23
Ren, F., Chen, X., Zhang, H., de Grijs, R., Deng, L., & Huang, Y. 2021, ApJ, 911, L20
Shahbaz, T., Watson, C., & Dhillon, V. 2014, MNRAS, 440, 504
Shao, D.-S., Tang, S.-P., Jiang, J.-L., & Fan, Y.-Z. 2020, Phys. Rev. D, 102, 063006
Steiner, A. W., Heinke, C. O., Bogdanov, S., Li, C. K., Ho, W. C., Bahramian, A., & Han, S. 2018, MNRAS, 476, 421
Sztajno, M., Fujimoto, M. Y., van Paradijs, J., Vacca, W. D., Lewin, W. H. G., Penninx, W., & Trumper, J. 1987, MNRAS, 226, 39
Tarenghi, M., & Reina, C. 1972, Nat. Phys. Sci., 240, 53
Tauris, T., et al. 2017, ApJ, 846, 170
Woosley, S. E., et al. 2004, ApJS, 151, 75
in't Zand, J. J. M., Cumming, A., van der Sluys, M., Verbunt, F., & Pols, O. 2005, A&A, 441, 675

A. Simulating the parallax precision of Cen X − 4 in future Gaia data releases

To simulate the uncalibrated parallax (π_1) precision of Cen X − 4 for a future Gaia data release, we made two assumptions: **(1)** Cen X − 4 is observed by Gaia at equal intervals; **(2)** $\sigma_k^i = \sigma_k^j$, ($k = \alpha, \delta$ and $i \neq j$), where σ_α^i and σ_δ^i stand for, respectively, the uncertainty of right ascension (RA) and declination at the i-th observation.

The observation interval is determined with Table 1 of Gaia Collaboration et al. (2016). At the ecliptic latitude of Cen X − 4 ($-14°1$), the number of observations is 63 over 5 yr, corresponding to an interval of 29 d. It appears from Table 2 that, for a specific target, $\sigma_\alpha/\sigma_\delta \approx \sigma_{\mu_\alpha}/\sigma_{\mu_\delta}$ (where σ_{μ_α} and σ_{μ_δ} represent uncertainty of μ_α and μ_δ, respectively), which implies the ratio of spatial resolution between RA and declination deviates slightly from unity and changes with pointing. Hence, we set $\sigma_\alpha^i/\sigma_\delta^i$ to 1.21, which is the $\sigma_{\mu_\alpha}/\sigma_{\mu_\delta}$ of Cen X − 4 from EDR3.

Simulated positions of Cen X − 4 were generated with pmpar (available at https://github.com/walterfb/pmpar) using the 'predictor mode', based on the astrometric parameters of Cen X-4 in Table 2. We first simulated positions from MJD 56863 to

MJD 57901 (the observing period of EDR3). The sole variable σ_α^i (and σ_δ^i accordingly) was tuned to make the parallax precision equal to 0.13 mas, the current parallax precision of Cen X − 4. Subsequently, we stuck to the position uncertainties while extending the observing period to MJD 58689 (around the end day of the 5-yr period) and MJD 60516 (an indicative day 10 years after the first light of Gaia), which, respectively, yield parallax uncertainties of 0.095 mas and 0.067 mas. Thus, we predict the parallax precision of Cen X − 4 to improve by a factor of 1.3 and 1.9, respectively, with DR4 and 10-yr data. Besides, we expect the proper motion precision of Cen X − 4 to be enhanced by 2.7 and 6.7 times, respectively, with DR4 and 10-yr data.